applied sciences

MDPI

Article

Multi-Objective Optimization Strategy for Commercial Vehicle Permanent Magnet Water Pump Motor Based on Improved Sparrow Algorithm

Wenjun Pei [1,2], Ping Xiao [1,3,*], Jiabao Pan [1,2], Zhihao Li [1,2] and Aoning Lv [2]

[1] Anhui Province Key Laboratory of Intelligent Car Wire-Controlled Chassis System, Anhui Polytechnic University, Wuhu 241000, China; 2220110151@stu.ahpu.edu.cn (W.P.); panjiabao@ahpu.edu.cn (J.P.); 2220110119@stu.ahpu.edu.cn (Z.L.)
[2] School of Mechanical and Automotive Engineering, Anhui Polytechnic University, Wuhu 241000, China; 18110850667@163.com
[3] School of Engineering, University of Bridgeport, Bridgeport, CT 06604, USA
* Correspondence: tlxp95@ahpu.edu.cn

Abstract: In order to achieve multi-objective optimization for a permanent magnet water pump motor in heavy commercial vehicles, we propose a strategy based on response-surface methodology and the improved sparrow algorithm (CGE-SSA). Firstly, the output capacity of the pump during actual operation was tested with an experimental bench to determine the design parameters of the motor, and then its modeling was completed using Ansys Maxwell 2022r2 software. Secondly, the response-surface model was established by taking the parameters of permanent magnet width, rib width, and slot width as optimization parameters and the output torque (T_a), torque ripple (T_r), and back electromotive force (EMF) amplitude as optimization objectives. Meanwhile, three methods—namely, circular sinusoidal chaotic mapping, improved golden sinusoidal strategy, and adaptive weight coefficients—were used to improve the convergence speed and accuracy of the sparrow search algorithm (SSA). Finally, the multi-objective optimization of the permanent magnet synchronous motor was completed using the improved sparrow algorithm. A comparative analysis of the motor's output before and after optimization showed that the torque pulsation and reverse electromotive force of the motor were significantly improved after optimization.

Keywords: improved sparrow algorithm; permanent magnet pump motor; multi-objective optimization; operating condition analysis

check for updates

Citation: Pei, W.; Xiao, P.; Pan, J.; Li, Z.; Lv, A. Multi-Objective Optimization Strategy for Commercial Vehicle Permanent Magnet Water Pump Motor Based on Improved Sparrow Algorithm. *Appl. Sci.* **2024**, *14*, 9666. https://doi.org/10.3390/app14219666

Academic Editor: Alessandro Lo Schiavo

Received: 30 August 2024
Revised: 12 October 2024
Accepted: 14 October 2024
Published: 23 October 2024

Copyright: © 2024 by the authors. Licensee MDPI, Basel, Switzerland. This article is an open access article distributed under the terms and conditions of the Creative Commons Attribution (CC BY) license (https://creativecommons.org/licenses/by/4.0/).

1. Introduction

Water pumps are important to vehicular cooling systems, directly affecting the efficiency, fuel consumption, and emissions of the vehicle. Traditionally, water pumps have been controlled through mechanical drag, using the belt connected to the crankshaft of the motor to control the flow rate, but this method can cause problems such as a poor cooling effect, low efficiency, and high vehicle energy consumption [1–3]. More recently, e-water pumps have been shown to effectively improve the cooling effect, thereby saving fuel and reducing emissions [4–6]. Thus, with the advent of the new energy era, the application of electronic water pumps in the field of passenger cars has been very popular; however, in heavy commercial vehicles, their motor efficiency is low, so they are rarely used. At present, permanent magnet synchronous motors have many advantages, such as their small size, high power density, and high efficiency [7–9], and they are widely used in the field of electronic water pumps. Compared with passenger cars, water pump motors in commercial vehicles need to have greater power, with limited installation space and higher output performance requirements, thus imposing stricter requirements for their design and optimization.

In terms of motor design, the parameters are mainly determined according to the load requirements, and the design is completed with the help of simulation software [10,11]. The authors of ref. [12] determined pump motor design parameters, according to the performance parameters of electronic water pumps on the market, and then completed the optimized design using Ansys Maxwell RMxprt 2022r2 software and a genetic algorithm. In ref. [13], a permanent magnet brushless DC motor was modified, and the stator and rotor of the motor were redesigned to meet the flow demand of the water pump. The aforementioned study used the performance parameters of the water pump itself to determine the design parameters of its motor, without considering the actual cooling needs of the engine, so the motor was large in size and its output capacity was excessive, properties which are not beneficial to reducing cost and layout space.

Scholars studying motors both domestically and abroad have mainly achieved motor optimization through stator and rotor structure parameter optimization. The authors of ref. [14] used Taguchi's method to optimize the shape of the permanent magnet synchronous motor, and the results show that the optimized two-layer Machaon design has low torque pulsations. In ref. [15], the table-adhesive structure of bilateral-rotor permanent magnets was used to increase the air-gap magnetization, thus enhancing the output torque. The authors of ref. [16] studied the shape of surface-mounted rotor permanent magnets and used the pole-shaving method in order to generate effective magnetic density harmonics in the air gap and inject corresponding harmonic currents to enhance the output torque. The above studies predominantly focused on a single optimization objective, often overlooking the impacts on other aspects of the motor's performance.

In order to simultaneously take into account multiple performance indices for the motor, multi-objective optimization strategies have been proposed. For example, in ref. [17], the NSGA-II algorithm was used to achieve significant reduction in cogging torque, using the cogging torque and output torque as the optimization objectives. In order to increase the average thrust of the motor and reduce its fluctuation, the researchers in ref. [18] used a neural network to establish a motor agent model, and the Pareto frontier method was used to determine the optimal parameter range with which to complete the multi-objective optimization of the permanent magnet synchronous motor. The authors of ref. [19] proposed a novel agent-assisted multi-objective optimization algorithm, with permanent magnet synchronous motor torque pulsation, torque amplitude, and a permanent magnet as optimization objectives. In order to reduce the cogging torque and torque pulsation, the researchers in ref. [20] adopted Taguchi's method to optimize the magnetic poles of the permanent magnet synchronous motor and establish the parameter optimization matrix, and the optimization results showed that orthogonal matrix optimization not only effectively suppressed cogging torque and torque pulsation, but also improved the output torque. In ref. [21], a multi-objective optimization strategy was proposed, based on finite element analysis and a modified particle swarm optimization algorithm with efficiency, a weak magnetic rate, and price as the optimization objectives. The authors of ref. [22] proposed a heuristic structure optimization method for permanent magnet synchronous motors, using motor efficiency and cogging torque as optimization objectives. Most of the above studies required a large number of sampled data points to optimize the motor, an approach which has strong dependence on finite element analysis and suffers from low optimization efficiency.

However, the efficiency of multi-objective optimization for electric machines has been greatly improved with the proposed strategy of response-surface methodology combined with intelligent algorithms. In ref. [23], a multi-objective optimization design method was proposed, based on response-surface methodology and the particle swarm optimization algorithm, to improve the performance of levitation force and levitation force pulsation. The researchers in ref. [24] proposed a multi-objective hierarchical optimization strategy in order to improve the thrust and reduce the thrust pulsation of permanent magnet linear synchronous motors, adopting the CCD method to construct the response-surface model, in combination with the multi-objective particle swarm algorithm to complete the optimiza-

tion design. In ref. [25], a multi-objective optimization method was proposed, based on a combination of design parameter hierarchy and the response-surface method, using the maximum and minimum ant algorithms to obtain the optimal solution of the response-surface model in order to realize the optimization of cogging torque, torque pulsation, and average torque. The researchers in ref. [26] proposed a hybrid artificial bee colony algorithm, combined with a support vector mechanism for drive motor optimization, compared with the performance of the conventional algorithm in two mathematical test functions to verify its significant performance. In the aforementioned study, the local sensitivity formula was commonly used to approximate the sensitivity value when performing parameter sensitivity analysis, and the sampling points were generally small, resulting in problems such as strong randomness and imprecision in the calculation results and leading to an ultimately suboptimal effect.

In this paper, in order to address the problems of low efficiency and poor optimization with the traditional multi-objective optimization strategies for electric motors, we propose an optimization method based on the response-surface method and the improved sparrow algorithm. In contrast to the traditional determination methods for the design parameters of a pump motor, we take into account the cooling demand of the engine during actual operation, thereby effectively avoiding the problem of large motor volume design with excess output capacity. At the same time, we adopted improved Latin hypercubic sampling and the correlation coefficient method to calculate the parameter sensitivity, resulting in more accurate and universal calculations of parameter sensitivity and effectively improving the optimization effect. Moreover, in order to better solve the multi-objective optimization problem for permanent magnet pump motors, we adopted the improved sparrow algorithm to optimize the response-surface model. Therefore, we aimed to improve the randomness of the sparrow population's initialization distribution through the introduction of circular sinusoidal chaotic mapping; to achieve the optimization of the iterative modes of discoverer and follower through the use of improved golden sine strategy and uniformly distributed adaptive coefficients; and to address the shortcomings of the traditional sparrow algorithm that cause its results to easily fall into the local optimum, so as to improve the algorithm's convergence speed and optimization accuracy.

2. Analysis of Working Conditions and Motor Model Construction

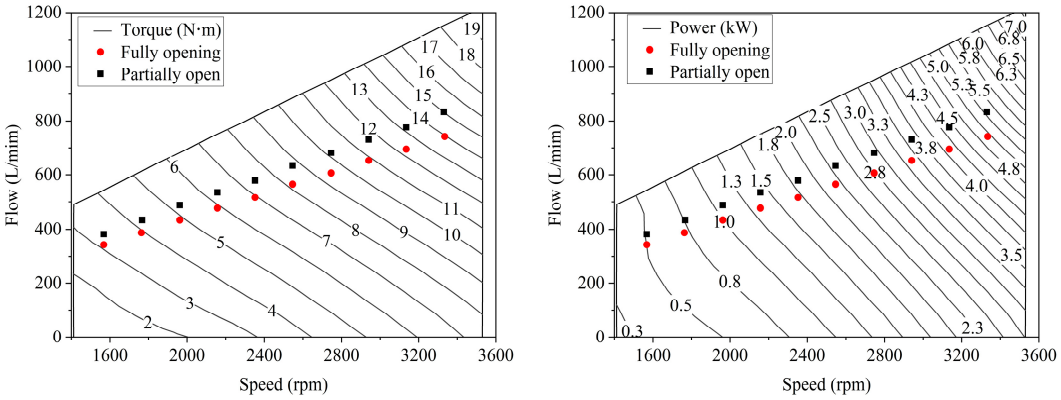
2.1. Analysis of Commercial Vehicle Water Pump Conditions

Traditional water pump motor design parameters are based on the maximum output capacity of the water pump, which is often at excess output capacity during the process of cooling the engine, thus leading to a too-large motor design. In order to solve this problem, we used the experimental bench test engine in different operating conditions under the water pump output flow; then, according to the water pump speed, the universal characteristic curve of flow under the operating conditions was used to calculate the water pump's power and torque in order to determine the motor design parameters. What follows is a set of engine water pump parameters and operating conditions for the calculated distribution of points, as shown in Table 1 and Figure 1.

Table 1 shows that the actual maximum flow rate of the pump is 833 L/min, lower than its maximum output flow rate of 1200 L/min, which verifies the problem of excess output capacity. In Figure 1a, it can be seen that, the greater the flow, the greater the input torque of the pump, so the torque at the 833 L/min working point is considered as the peak torque of the motor; combining this with the common speed of the engine, it can be seen that the common speed of the water pump with the thermostat fully open is 1764–2744 rpm, so we selected the speed of 2744 rpm for the motor's rated point. Thus, the motor's rated speed was determined to be 2800 rpm, with a rated power of 2.8 kW and a peak power of 5.2 kW.

Table 1. Water pump flow parameters.

Speed (rpm)	Flow (L/min)	
	Fully Opened	Partially Opened
1568	342	382.4
1764	387.8	433.8
1960	433.8	487.8
2156	477	536.3
2352	517.3	579.5
2548	565.9	633.4
2744	606.4	682
2940	652.1	730.5
3136	695.3	776.2
3332	741.3	833



(**a**) (**b**)

Figure 1. Water pump working condition data points: (**a**) pump torque operating points and (**b**) pump power operating points.

2.2. Motor Finite Element Modeling

According to the motor design parameters determined through the analysis of working conditions in Motor-CAD to complete the preliminary modeling of the motor, Maxwell-2D simulation and analysis were used to adjust the structural parameters and ultimately complete the model's construction. The motor model discussed in this paper is an 18-slot, 8-pole, built-in V + 1 permanent magnet synchronous motor, with three-phase winding connected in a star pattern, with parallel permanent magnet magnetization, which is conducive to improving the sinusoidal degree of the air-gap magnetic density waveform. The motor parameters and finite element model are shown in Table 2 and Figure 2.

Table 2. Motor parameters.

	Items	Unit	Value
Motor parameters	Rating power	kW	2.8
	Rating speed	rpm	2800
	Peak power	kW	5.2
	Peak speed	rpm	6000
	Peak torque	N·m	20.09
	Stator outer diameter	mm	146
	Stator inner diameter	mm	85
	Core length	mm	49
	Rated voltage	V	540
	Extremity	/	8
	Number of grooves	/	18

Table 2. *Cont.*

	Items	Unit	Value
Materials	Permanent magnet	/	N35SH
	Stator and rotor	/	DW310-35
Thermal parameters	Reference temperature	°C	20
	Demagnetization temperature	°C	150

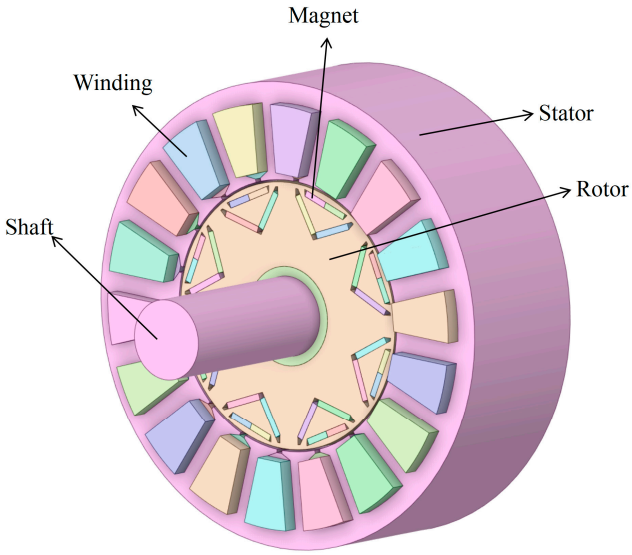


Figure 2. Three-dimensional finite element model.

3. Multi-Objective Optimization Design

Since there was more than one objective being used to determine the performance of the permanent magnet synchronous motor and strong coupling between the optimization objectives, it would not be possible to use the conventional single-objective optimization solving method considering multiple objectives at the same time, so a multi-objective optimization design is proposed. The multi-objective optimization of a permanent magnet synchronous motor mainly includes four parts: selection of optimization parameters and optimization objectives, sensitivity analysis, response-surface modeling, and multi-objective optimization based on the improved sparrow algorithm (CGE-SSA). The multi-objective optimization flow chart is shown in Figure 3.

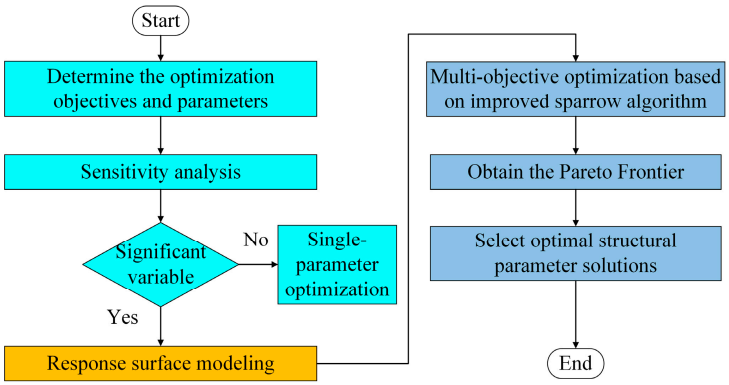


Figure 3. Optimization flow chart.

3.1. Optimization Objectives and Parameters

In order to improve the output stability and smoothness of the built-in permanent magnet synchronous motor, as well as the overall efficiency of the motor under the condition of satisfying the output, a multi-objective optimization strategy is proposed here. Since reducing the torque pulsation can effectively reduce noise and vibration, and appropriately increasing the reverse electromotive force can effectively improve the motor efficiency, the torque ripple (T_r), output torque (T_a), and back EMF amplitude (E) were taken as the optimization objectives, and seven structural parameters were selected as the optimization parameters. Table 3 shows the names and value ranges of the optimization parameters, and Figure 4 shows the optimization variable diagram. Usually, when the torque ripple of the permanent magnet synchronous motor is less than 5%, the motor output is smoother; thus, considering that the output torque of the initial motor model is 9.7 Nm, and its back EMF amplitude is 245 V, in order to better improve the performance of the motor and satisfy the optimization requirements with the set of solutions obtained through algorithm optimization, the multi-objective optimization problem, as well as its constraints, can be expressed as follows:

$$\min \begin{cases} f_1(x) = -T_a \\ f_2(x) = T_r \\ f_3(x) = -E \end{cases} \tag{1}$$

$$T_a > 9.7 \text{ Nm}, E > 245 \text{ V}, T_r < 5\% \tag{2}$$

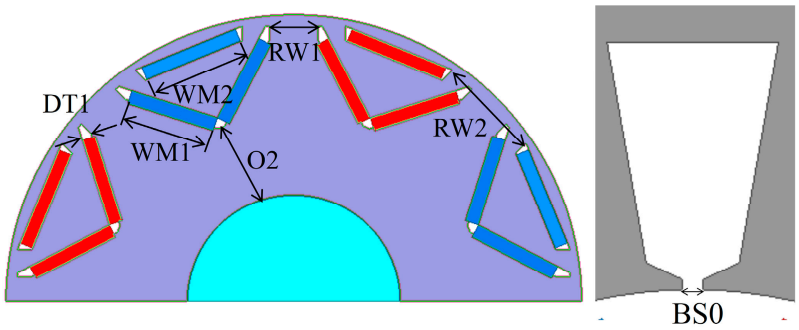


Figure 4. Optimization variable map.

Table 3. Optimization variables.

Name	Parameter	Unit	Starting Value	Range
Rib Width 1	RW1	mm	4	4~7
Duct 1 thickness	DT1	mm	1.4	1~2
Width of Permanent Magnet 1	WM1	mm	28	25~30
Distance from duct bottom to shaft Surface	O2	mm	10	8~12
Rib Width 2	RW2	mm	14	11~15
Width of Permanent Magnet 2	WM2	mm	14	11~15
Slot opening width	BS0	mm	2	1.8~2.2

3.2. Sensitivity Analysis of Optimized Parameters

Since there were seven parameters to optimize, increasing the complexity of the test and affecting the accuracy of the optimization, a sensitivity analysis is proposed, with the aim of reducing the test's overall workload and improving the optimization accuracy. In this study, we chose to improve the Latin hypercube, sampling 100 sampling points, use Ansys Optislang 2022r2 software to test the degree of influence of parameter changes on the optimization objective (sensitivity), and use Spearman correlation coefficients to evaluate the sensitivity value.

Improved Latin hypercube sampling is mainly divided into three steps: stratification, sampling, and disorder. The specific steps are as follows:

(1) Determine the number of samples N and the dimension D to be sampled, and divide each dimension into N equal parts to obtain N values to be taken, denoted as V_1, V_2, …, V_N;
(2) For the first dimension, randomly take a number from V_1, V_2, …, V_N as the first sample value, remove it from the list, and then repeat for further sample values until the value of the Dth dimension is removed;
(3) Finally, the obtained samples are discharged in columns to form a matrix of N rows and D columns, which is noted as the Latin hypercube sample matrix.

Considering that the relationship between optimization objectives and design variables in the motor is more complex, the sampling points were selected with non-normal distribution; as such, it would be more rough to judge the sensitivity using a linear relationship, so the Spearman coefficient was used to describe the convergence between the objectives and the variables, as it does not require the sampling data to be normally distributed. Therefore, the correlation coefficient sensitivity analysis formula is as follows [27]:

$$S(x) = \frac{\sum_{i=1}^{N}(x_i - \overline{x})(Y_i - \overline{Y})}{\sqrt{\sum_{i=1}^{N}(x_i - \overline{x})^2}\sqrt{\sum_{i=1}^{N}(Y_i - \overline{Y})^2}} \tag{3}$$

where x_i and Y_i are the design parameter values and design objective values of the ith sampling point; $\overline{x}$, and $\overline{Y}$ are the design parameter average and design objective average; and N is the number of sampling points.

Since it was necessary to study the influence of a single parameter on multiple optimization objectives, we introduced a comprehensive sensitivity formula. Considering that permanent magnet synchronous motors have high requirements on torque ripple, and, at the same time, torque ripple serves as an important measure of motor output performance, weighting coefficients were introduced to reflect the importance of different optimization objectives, so as to ensure that the parameters that have greater impacts on torque ripple can be retained. The integrated sensitivity formula is as follows [28]:

$$G_x = \gamma_1 S_1(x_i) + \gamma_2 S_2(x_i) + \gamma_3 S_3(x_i) \tag{4}$$

where G_x is the integrated sensitivity; S_1, S_2, and S_3 are the sensitivities of T_r, E, and T_a, respectively; and γ_1, γ_2 and γ_3 are the corresponding weighting coefficients, which take the values of 0.4, 0.3, and 0.3, respectively.

The results of the sensitivity analysis are shown in Figures 5 and 6. The sensitivity values of RW1, WM1, RW2, and WM2 are the highest, and therefore have the greatest impacts on the optimization objective, so they were defined as high-sensitivity parameters, while the remaining three were considered low-sensitivity parameters. The high-sensitivity parameters were optimized using CGE-SSA, and the low-sensitivity parameters were optimized in a parametric way.

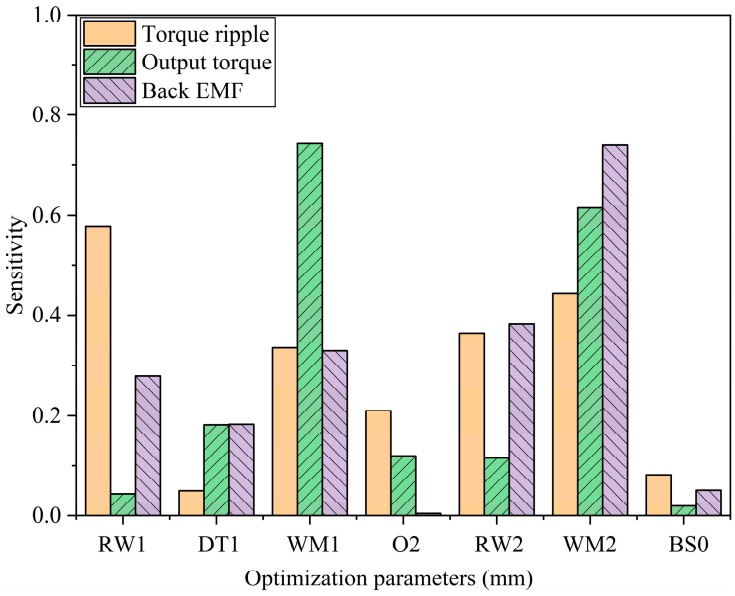


Figure 5. Sensitivity analysis.

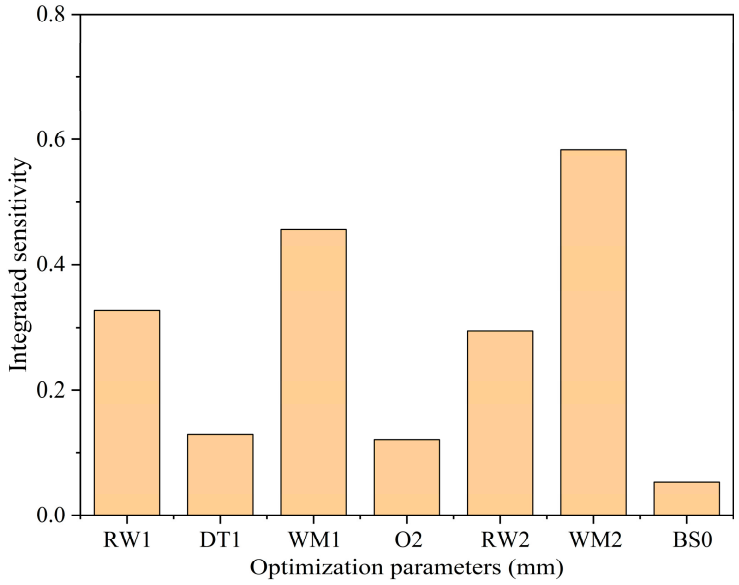


Figure 6. Integrated sensitivity analysis.

4. Response-Surface Modeling

Response-surface methodology (RSM) is a common multi-objective optimization model, which is widely used in materials-related fields and has also been applied to motor optimization in recent years. In order to obtain the relationships between the optimization parameters and the optimization objectives, we tested the modeling accuracy of different regression equations to build a response surface in the software Design Expert 13, through which it was concluded that quadratic polynomial response-surface modeling had the highest accuracy, with variance above 0.9. Therefore, in this study, the quadratic polynomial method was chosen to establish the response-surface model, the formula for which is as follows [29]:

$$f(x) = \beta_0 + \beta_i \sum_{i=1}^{k} x_i + \beta_{ii} \sum_{i=1}^{k} x_i^2 + \beta_{ij} \sum_{i<j}^{k} x_i x_j + \varepsilon \quad (5)$$

where β_0 is the constant term; β_i is the first-order coefficient; β_{ii} is the second-order coefficient; β_{ij} is the interaction term coefficient; and ε is the error constant.

In order to reduce the experimental volume, we adopted the Box–Behnken Design (BBD) test method to establish the response-surface model. The BBD method classifies individual parameters into three levels (−1, 0, and 1), with 0 representing the center point and −1 and 1 representing the lowest and highest levels, effectively reducing the number of finite element methods [30]. First, a 3-level, 4-factor experimental model was established using the BBD experimental method in Design Expert 13 software, and then Ansys Maxwell 2022r2 software was used to complete the simulation calculation for 29 groups of experiments; finally, the second-order regression equation was chosen to establish the response-surface model and analyze the model's accuracy. The parameters and significance levels are shown in Table 4.

Table 4. Parameters and significance levels.

Parameter/Level	−1	0	1
RW1	4 mm	5.5 mm	7 mm
WM1	25 mm	27.5 mm	30 mm
RW2	11 mm	13 mm	15 mm
WM2	11 mm	13 mm	15 mm

The results of the target model evaluation are shown in Table 5, in which the signal-to-noise ratios of the output torque, back EMF amplitude, and torque ripple quadratic models are all greater than 4 dB, the variances are all greater than 0.9, and the CVs are all less than 10%, thus proving that the tests are highly credible and accurate, and suggesting that the response-surface model can adequately describe the relationships between the variables and the target variables. In Figure 7, which illustrates the response-surface model plots of optimization parameters and objectives, it can be seen that all three response-surface models have extreme values, where the optimization parameters have optimal ranges, but they are different for each model. Therefore, in order to avoid conflicts between the optimization objectives, it was necessary to use the multi-objective optimization algorithm to obtain the optimal solution set.

Table 5. Assessment results.

Optimization Goal	Model	R^2	CV (%)	Signal-to-Noise Ratio (dB)
Output torque	Quadratic	0.99	0.1	242.12
Torque ripple	Quadratic	0.92	6.3	13.46
Back EMF amplitude	Quadratic	0.99	0.38	59.45

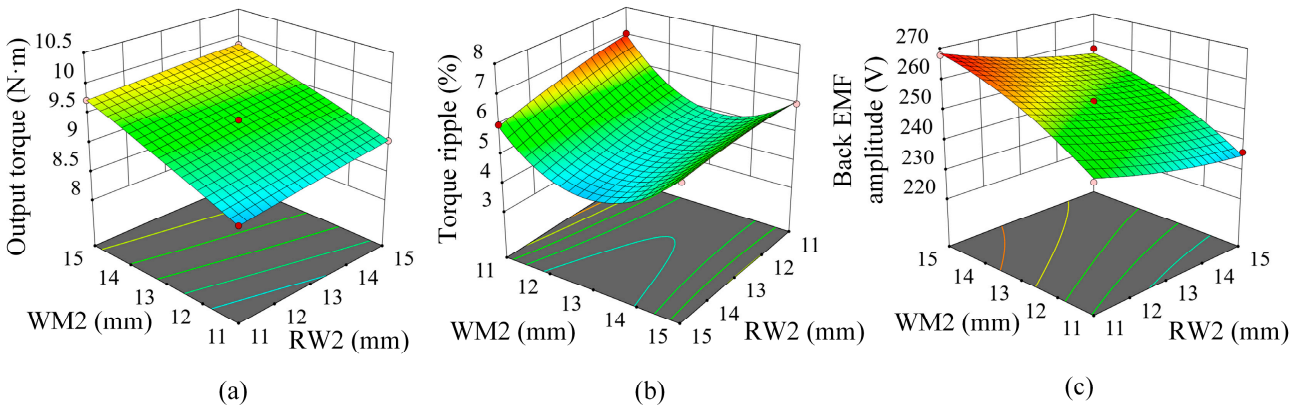


Figure 7. Response-surface model: (**a**) output torque; (**b**) torque ripple; and (**c**) back EMF amplitude.

5. CGE-SSA Multi-Objective Optimization

5.1. Algorithmic Principle

The sparrow search algorithm was proposed by Jiankai Xue et al. in 2020 [31], as an intelligent optimization algorithm based on the characteristics of sparrows when searching for food and avoiding enemies. The sparrow population mainly consists of discoverers, followers, and scouters. The algorithm is used to perform local and global optimization searches by mimicking the sparrow's foraging and anti-predator behaviors, in which the discoverer's main task is to search for food, the follower will quickly fly to the discoverer's position when food is found, and scouters are responsible for scouting to deliver early warnings and will abandon food when in danger. This algorithm has the advantages of a fast convergence speed and high optimization accuracy compared to traditional algorithms; however, the traditional sparrow algorithm still faces the problems of uneven population initialization distribution, easily falling into the local optimum, poor global search ability, etc. Therefore, in this study, we carried out the following three improvements in order to address the shortcomings of the traditional sparrow algorithm and improve the algorithm's convergence speed and accuracy.

5.2. Improved Sparrow Algorithm

5.2.1. Circular Sinusoidal Chaotic Mapping Strategy for Population Initialization

The traditional SSA adopts random generation for the initialized sparrow population, which can then easily fall into the local optimum. Sinusoidal chaotic mapping can solve this drawback of the algorithm, in addition to its slow convergence speed [32]. In this study, we combined circular chaotic mapping with sinusoidal chaotic mapping, thus making the initialized sparrow distribution more uniform, as well as improving the convergence speed and computational accuracy of the algorithm. Circular sinusoidal chaotic mapping uses weight coefficients to combine circular and sinusoidal mapping to form a new function, as shown in Equation (6). The strategy is first used to generate random values from $X(i)$, then Equation (6) is used to generate chaotic values. Finally, the chaotic values are mapped to individual sparrows in order to achieve sparrow population initialization.

$$X(i+1) = \mathrm{mod}\left(X(i) + b - \frac{a}{2\pi}\sin(2\pi X(i)) + \omega \cdot c \cdot \sin(\pi X(i)), 1\right) \quad (6)$$

where mod denotes the residual function; $X(i)$ is a random sequence, $X(i) \in [lb, ub]$; ub and lb are the upper and lower bounds of the search space, respectively; $X(i+1)$ is the chaos value, $X(i+1) \in [lb, ub]$; a, b, and c are the control parameters, taken as 0.16, 0.556, and 0.24, respectively, after testing and comparing; and ω is the weight coefficient, which takes the value of 0.2 after testing and comparing.

In order to verify the superiority of the circular sinusoidal chaotic mapping strategy for initializing the population, the population number was set to 200, and the sparrow population was initialized in the two-dimensional space. The random distribution and circular sinusoidal chaotic mapping population distribution are shown in Figure 8. In the figure, it can be seen that the population initialized with the circular chaotic mapping strategy has a more uniform distribution, and there is no positional repetition, which is conducive to preventing the algorithm from falling into a local optimum during the optimization process.

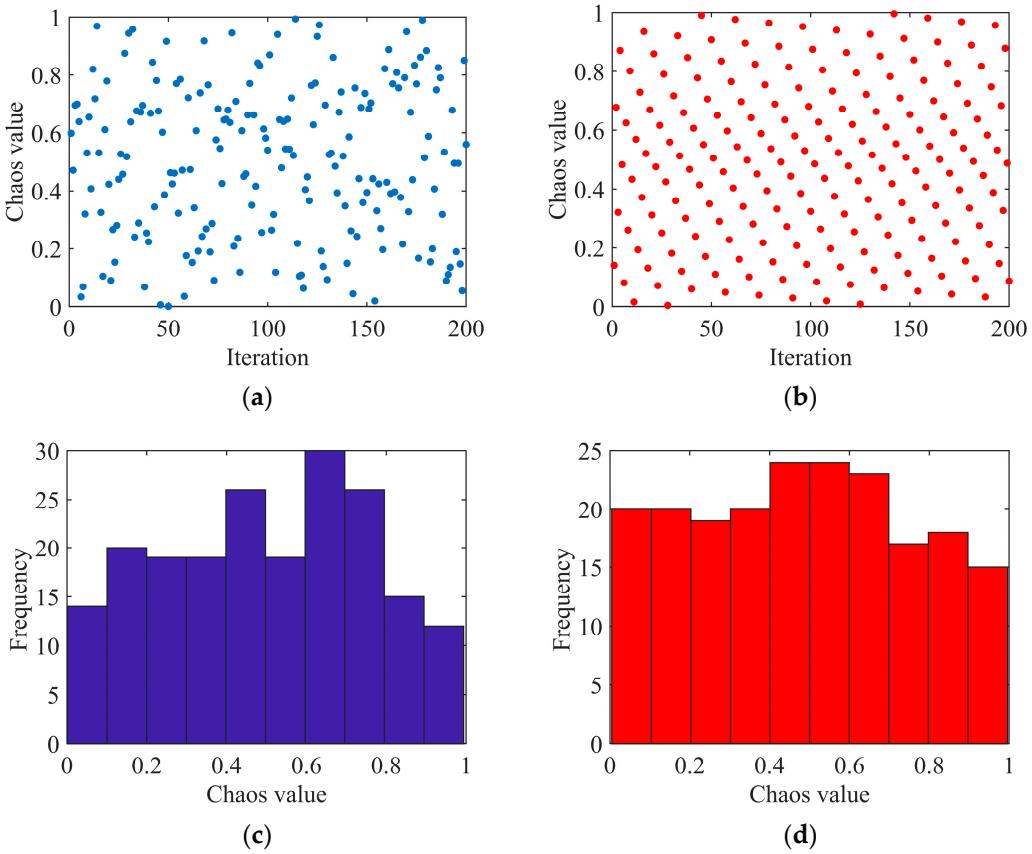


Figure 8. Population distribution map: (**a**) random population distribution; (**b**) circular sinusoidal chaos map population distribution; (**c**) histogram of randomized population distribution; and (**d**) histogram of circular sinusoidal chaotic mapping population distribution.

5.2.2. Improved Gold Sine Strategy Update Discovery

The traditional SSA finder position updating process is prone to premature convergence into local optimization; to solve this problem, a sinusoidal function was used for the optimization search, thus expanding the search space of the algorithm and improving its global optimization ability. The golden section coefficient was also introduced to enable the algorithm to search more fully in the local region, in order to avoid falling into local optimality [33]. In order to make it easier for the algorithm to move beyond the local optimal solution and explore a wider solution space, the optimal solution perturbation strategy was added to the golden sine search. The improved finder update formula is as follows:

$$X_{i,j}^{t+1} = \begin{cases} X_{i,j}^{t} \cdot |\sin(r_1)| + r_2 \cdot \sin(r_1) \cdot \left| x_1 \cdot X_{best1}^{t} - x_2 \cdot X_{i,j}^{t} \right| & \text{if } R < ST \\ X_{i,j}^{t} + Q \cdot L & \text{if } R \geq ST \end{cases} \tag{7}$$

$$X_{best1}^{t} = X_{best}^{t} + \left| X_{i,j}^{t} - X_{best}^{t} \right| \cdot A^{+} \cdot L \tag{8}$$

where $X_{i,j}$ is the position of the sparrow; X_{best} is the global optimal position; X_{best1} is the global optimal position after the perturbation; Q is a random number obeying a normal distribution; $r_1 \in [0, 2\pi]$ and $r_2 \in [0, \pi]$ are random numbers determining the distance and direction of motion of the individual for the next iteration, respectively; $x_1 = -\pi + 2\pi(1 - \tau)$, $x_2 = -\pi + 2\pi\tau$ are the coefficients obtained based on the golden section coefficient τ; $\tau = \left(\sqrt{5} - 1\right)/2$; L is a $1 \times$ dim matrix whose elements are all 1; and $A^{+} = A^{\mathrm{T}} \left(AA^{\mathrm{T}}\right)^{-1}$, where A is a $1 \times$ dim matrix with elements -1 or 1.

In order to verify that the sinusoidal function can expand the search space, and thus improve global optimization ability, the benchmark test function f_{10} was used to compare the optimization ability of the algorithm with and without the sinusoidal function [34]. The number of populations was set to 100, the maximum number of iterations to 100, with the cycle recurring 50 times, and the function f iteration curve is shown in Figure 9, where it can be seen that, when there is a sinusoidal function, the iteration curve converges to 8.88×10^{-16}; meanwhile, when there is no sinusoidal function, the iteration curve does not converge, and the optimal value of the search is 1.01×10^{-5}. It can thereby be concluded that the position updating formula can effectively improve the algorithm's convergence speed and accuracy when there is a sinusoidal function.

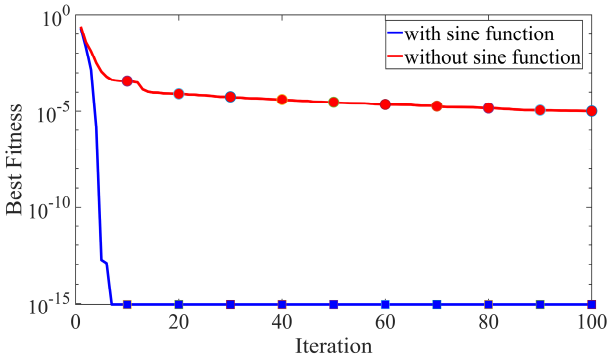


Figure 9. Function f_{10} iteration curve.

When $R \geq ST$, some sparrows have found the danger, at which point the discoverer moves randomly to the neighborhood of the current position, according to a normal distribution, and conducts a local search. When $R < ST$, the global optimal position is not a fixed value, and adding random perturbation to increase the search range allows the finder to further expand the search space under the effect of the golden sine strategy in order to conduct a global search.

5.2.3. Dynamic Adaptive Weight Improvement Follower with Uniform Distribution

During the optimization process for the traditional SSA, defects such as weak global search ability, weak local development, and easily falling into local optimization result in insufficient search accuracy. Therefore, drawing on the traditional idea that inertia weights can improve an algorithm's global search capability [35], uniformly distributed dynamic adaptive weights are proposed to coordinate the algorithm's global search and local exploitation capabilities. The improved follower position update formula is as follows:

$$X_{i,j}^{t+1} = \begin{cases} \beta \cdot Q \cdot \exp\left(\frac{X_{worst}^{t} - X_{i,j}^{t}}{i^2}\right) & i > \frac{n}{2} \\ X_p^{t+1} + \left|X_{i,j}^{t} - X_p^{t+1}\right| \cdot A^{+} \cdot L & i \leq \frac{n}{2} \end{cases} \tag{9}$$

$$\beta = \delta\left(\beta_{initial} - \left(\beta_{initial} - \beta_{final}\right)\frac{1}{\exp(1) - 1}\right)\left(\exp\left(\frac{t}{T}\right) - 1\right) \tag{10}$$

where X_p is the optimal position found via the sender; X_{worst} is the worst position found via the discoverer; β is the dynamic weight; δ is a uniformly distributed random number from 0 to 1; $\beta_{initial}$ and β_{final} are the initial and ending values of the weight, which are taken as 1 and 0, respectively; and T is the maximum number of iterations.

In Figure 10, it can be seen that, in the pre-search phase of the algorithm, the dynamic weight is high, and the follower performs a global search using Equation (9). As the number of iterations increases, the value of dynamic weight becomes smaller, and the follower performs local exploitation. It is concluded that dynamic adaptive weighting improves the algorithm's global search and local development capabilities.

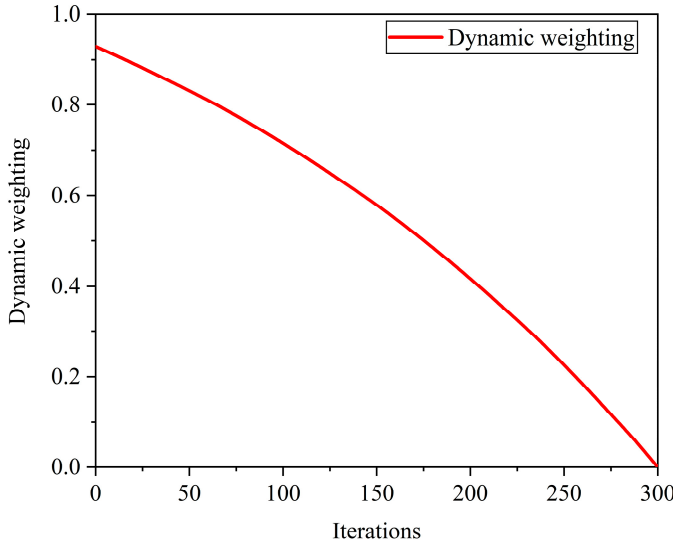


Figure 10. Dynamic weight change curves.

5.2.4. Simulation Verification

In order to verify the effectiveness of CGE-SSA, six test functions (three single-peak functions and three multi-peak functions) were selected to test CGE-SSA's global solving ability and the ability to move away from the local optimum by comparing it with the SSA, the genetic algorithm (GA), and the particle swarm algorithm (PSO). The test functions are described in Table 6.

Table 6. Test functions.

Function	Dim	Range
$f_1 = \sum_{i=1}^{n} x_i^2$	30	$[-100, 100]$
$f_2 = \sum_{i=1}^{n} \lvert x_i \rvert + \prod_{i=1}^{n} \lvert x_i \rvert$	30	$[-10, 10]$
$f_3 = \sum_{i=1}^{n} \left(\sum_{j-1}^{i} x_j \right)^2$	30	$[-100, 100]$
$f_4 = \sum_{i=1}^{n} -x_i \sin\left(\sqrt{\lvert x_i \rvert} \right)$	30	$[-500, 500]$
$f_5 = \left(\frac{1}{500} + \sum_{j=1}^{25} \frac{1}{j + \sum_{i-1}^{2} \left(x_i - a_{ij} \right)^6} \right)^{-1}$	2	$[-65.536, 65.536]$
$f_6 = -\sum_{i=1}^{5} \left[(x - a_i)(x - a_i)^T + c_i \right]^{-1}$	4	$[0, 4]$

The results of 50 experiments are shown in Table 7 and Figure 11. In Figure 11a–c, all three functions are single-peaked functions, so the iteration curves of the algorithms are closer. In Figure 11a–d, it can be seen that the iterative curves produced using the four functions of CGE-SSA converge at the 22nd, 21st, 25th, and 28th generations, respectively. The four function iteration curves produced using SSA do not converge, and the last generation results are 2.3×10^{-67}, 1.6×10^{-30}, 3.09×10^{-41}, and -7874.28. The f_1, f_2, and f_3 function curves produced using GA converge, and the convergence results are 30,717, 69.7, and 59,675. The f_1 and f_2 function curves produced using PSO also converge, and the convergence results are 21.3 and 20.06. As can be seen in Figure 11c,d, the convergence speed and accuracy of the CGE-SSA iterative curves are significantly higher than those of other algorithms.

Table 7. Comparison of experimental results.

Function	Parameter	SSA	CGE-SSA	GA	PSO
f_1	AVG	2.3×10^{-67}	0	30,717	21.3
	STD	1.2×10^{-66}	0	8176.9	2.63
f_2	AVG	1.6×10^{-30}	0	69.7	20.06
	STD	1.1×10^{-29}	0	10.7	1.9
f_3	AVG	3.09×10^{-41}	0	59,675	621.9
	STD	2.12×10^{-40}	0	19,941	296.2
f_4	AVG	−7874.28	−8500.69	−2286	−3989
	STD	604.83	517.46	464.9	417.6
f_5	AVG	4.66	1.4	1.63	2.34
	STD	5.1	0.83	1.38	1.93
f_6	AVG	−7.90	−10.1532	−0.8	−4.14
	STD	2.55	7.76×10^{-7}	0.43	2.4

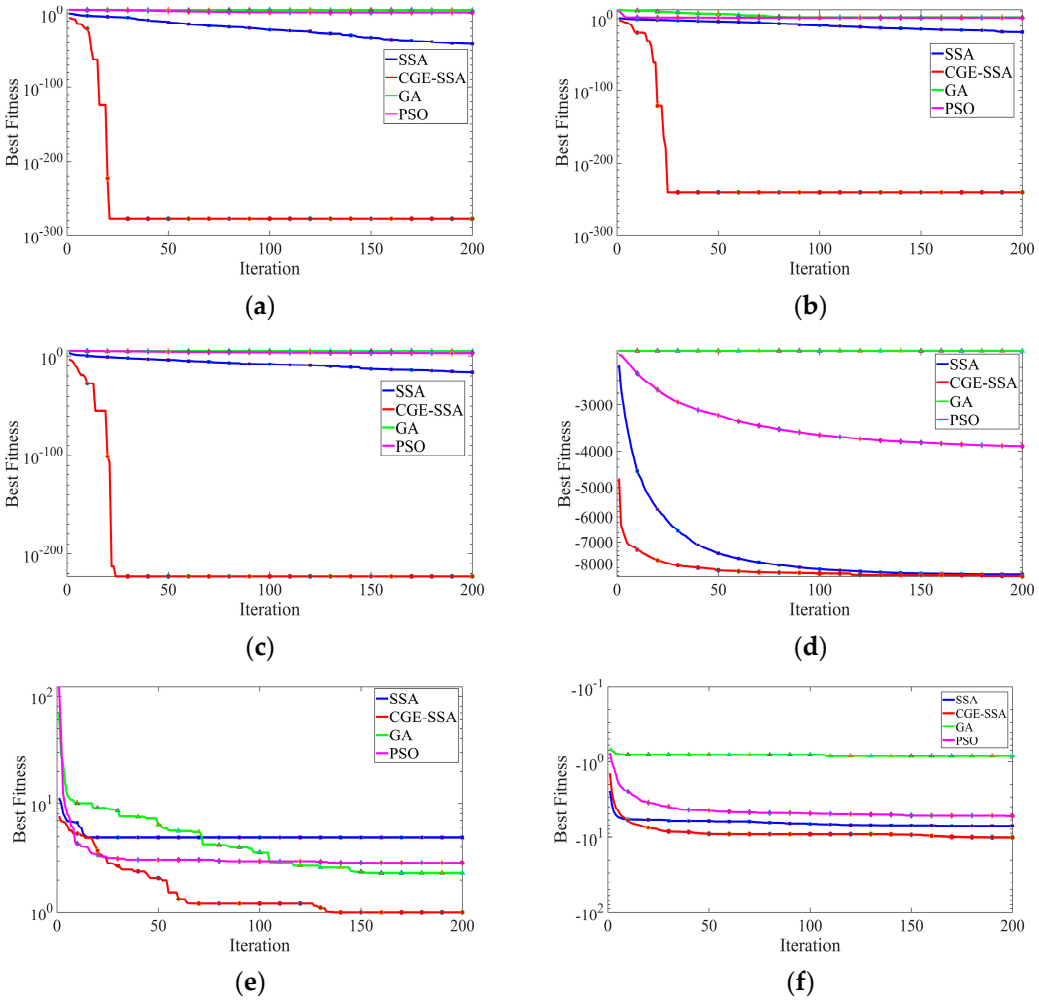


Figure 11. The convergence curves of test functions: (**a**) f_1; (**b**) f_2; (**c**) f_3; (**d**) f_4; (**e**) f_5; and (**f**) f_6.

The comparison of the convergence curves of each test function and the experimental results show that CGE-SSA has a better convergence speed and accuracy than SSA, GA, and PSO, and the standard deviation and mean of optimal fitness are smaller; the optimization effect of CGE-SSA is far better than those of the other algorithms, especially in the single-peak function, thus reflecting the superiority and stability of CGE-SSA. In summary, CGE-SSA shows improvement in terms of both optimization search time and global search ability compared with other algorithms.

5.3. CGE-SSA Multi-Objective Optimization

In contrast to the single-objective algorithm, the fitness values of individuals in the multi-objective algorithm are determined through multiple indicators, which cannot be directly compared to derive the optimal individual. Therefore, by adding a non-dominated sorting procedure and a congested space calculation procedure to CGE-SSA, the comparison of fitness values between multi-objective individuals is realized, and the non-dominated solution set is output to form an improved multi-objective sparrow search algorithm, the optimization flowchart of which is shown in Figure 12.

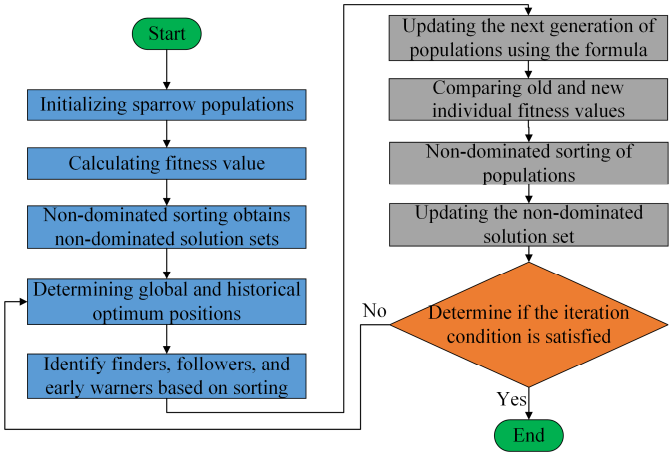


Figure 12. Algorithm optimization flowchart.

In this study, the second-order regression equation between the parameters of the optimization structure and the optimization objective was fitted through response-surface analysis, the improved multi-objective sparrow algorithm program was written using MATLAB R2018b software, and then the fitted objective function was written into the program to define the upper and lower limits of each parameter, as well as the constraints of the optimization objective. After setting the dimension to 4, the number of sparrow populations to 50, the non-dominated solution set repository to 50, and the maximum number of iterations to 200, the optimization objective was optimized to obtain the Pareto frontier, the result of which is shown in Figure 13.

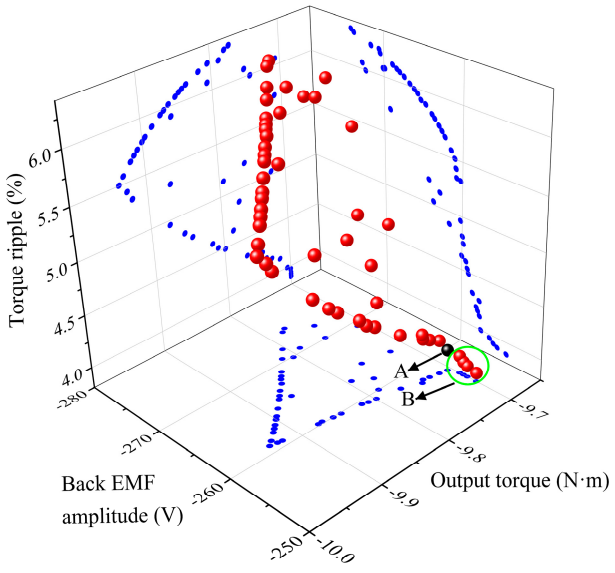


Figure 13. Pareto frontier.

According to the optimization objective and its constraints, set in Section 2.1, five optimal solutions were obtained, shown as point A and region B in the Pareto frontier chart. Among them, both point A and region B satisfy the requirement that the output torque is greater than 9.7 Nm, and the output torque of point A is slightly higher than that of region B. In addition, the torque ripple values at neither point A nor region B exceed 4%, which indicates a good output stability. Compared with the torque ripple and the output torque, the back EMF amplitude at point A differs greatly from that in region B, reaching 257.5 V. Therefore, point A was taken as the optimal solution point.

As can be seen in Table 8, within the reasonable variation range of the structural parameters, the optimized motor models using the four algorithms meet the requirements of the optimization objectives, and the torque ripple and back EMF amplitude are significantly improved, compared to the pre-optimization results, in terms of satisfying the output. Compared with the optimization results of SSA, GA, and PSO, the motor optimized with CGE-SSA has a lower torque ripple, higher back EMF amplitude, and higher output torque. In Figure 14, it can be seen that the magnetization density amplitude of the stator tooth part is about 1.6 T, and that of the yoke part is about 1.3 T, after optimization with CGE-SSA, and the magnetization density distribution is good; meanwhile, the rotor spacer bridge is saturated with magnetic density near the spacer bridge, which can effectively suppress magnetic leakage. Therefore, CGE-SSA demonstrates better optimization results than SSA, GA, and PSO, resulting in a better output performance for the optimized motor.

Table 8. Comparison of the results before and after optimization.

Parameter	Unit	Initial	CGE-SSA	SSA	GA	PSO
RW1	mm	4	7	5.9	6	6.2
DT1	mm	1.4	2	2	2	2
WM1	mm	28	28	26.8	26	27
O2	mm	10	9.5	11	11	10.5
RW2	mm	14	15	14	15	15
WM2	mm	14	13.69	14	14	13.7
BS0	mm	2	2	2	2	2
Back EMF amplitude	V	245.9	265.1	260.6	256.5	258.6
Output torque	N·m	9.7	10.31	10.02	9.94	10.14
Torque ripple	%	6.62	3.11	4.9	4.27	3.92

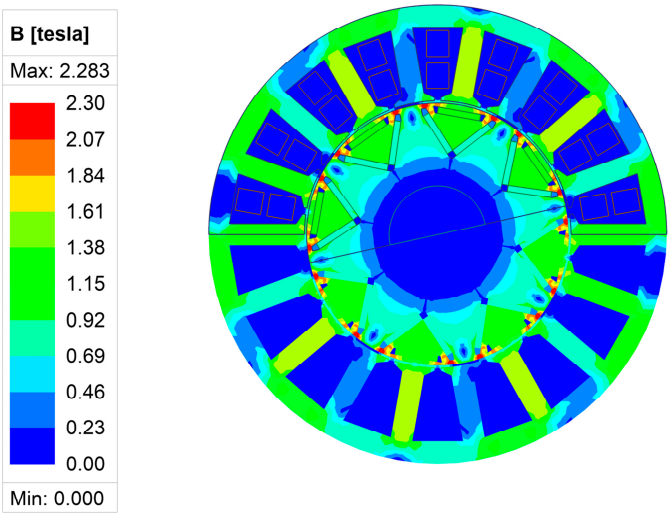
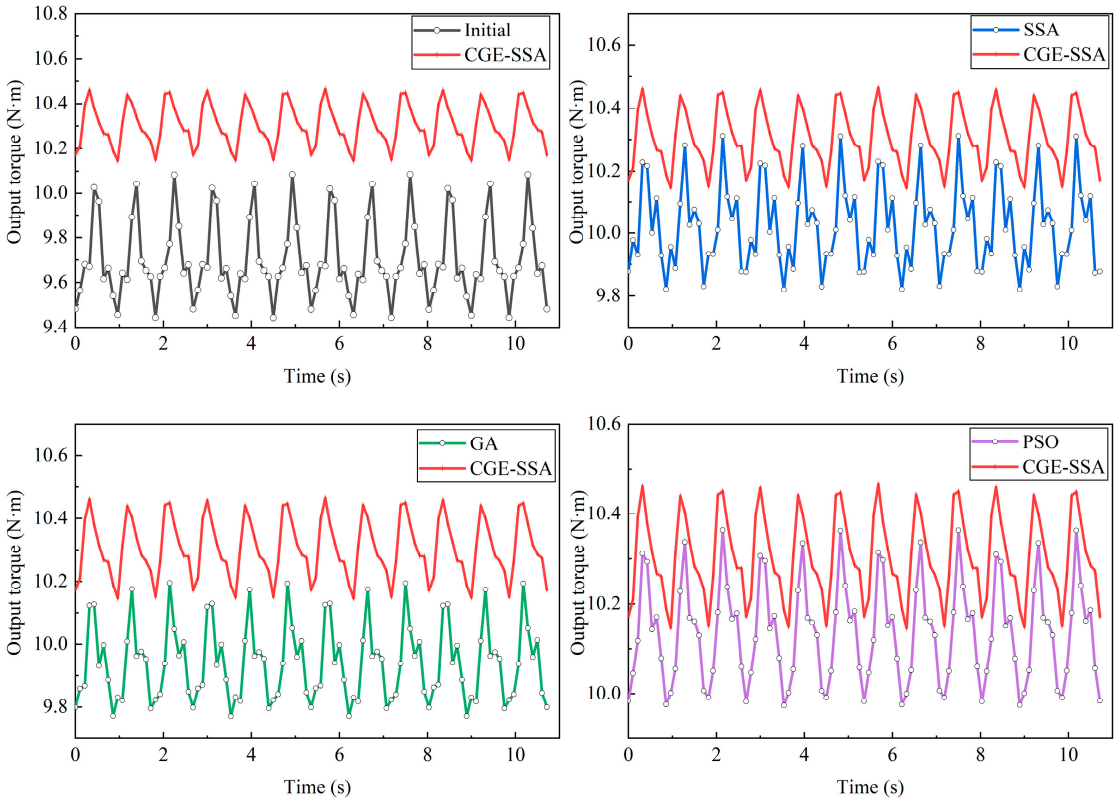


Figure 14. No-load magnetic density distribution.

As can be seen in Figure 15a, the red curve sits above the other curves, demonstrating that the average output torque after optimization using CGE-SSA is higher than those after optimization using the SSA, GA, or PSO, with levels of 10.31 Nm, 10.02 Nm, 9.94 Nm, and

10.14 Nm, respectively (all increased from the initial value of 9.7 Nm, which satisfies the output requirements), and that the average output torque after optimization using torque fluctuation is lower after optimization using CGE-SSA. It is thus proven that, compared with other algorithms, the output of the motor optimized with CGE-SSA is smoother, and the optimization effect is more obvious. Compared with the pre-optimization motor, the torque ripple of the motor after CGE-SSA optimization decreased, from 6.62% to 3.11%, a decrease of 53%. In Figure 15b,c, it can be seen that, compared with SSA, GA, and PSO optimization, the reaction potential amplitude of the CGE-SSA-optimized motor is higher and its distortion rate is lower. Compared with the initial motor, the back EMF amplitude increased, from 245.2 V to 265.01 V, an increase of 19.81 V. The fundamental amplitude increased, from 268 V to 273 V; the 3rd harmonic decreased from 24.8 V to 8.2 V; and the distortion rate decreased, from 9.2% to 3.8%, a decrease of 58.7%. The increase in the reaction potential can effectively improve the overall efficiency of the motor, and the decrease in the distortion rate can improve the sinusoidal degree of the reaction potential waveform, thus improving the stability of the motor output. As shown in Figure 15d, the cogging torque of the CGE-SSA-optimized motor is greatly reduced, which is similar to the result after optimization using PSO. Compared with the initial motor, the cogging torque amplitude decreased, from 98.7 mNm to 44.1 mNm, a decrease of 55%, which would greatly reduce the vibration and noise of the motor. The above comparative analysis proves that the optimization effect of CGE-SSA is better than those of the SSA, GA, and PSO, and the smoothness of the optimized motor output is significantly improved, with a better overall output performance.



(**a**)

Figure 15. *Cont.*

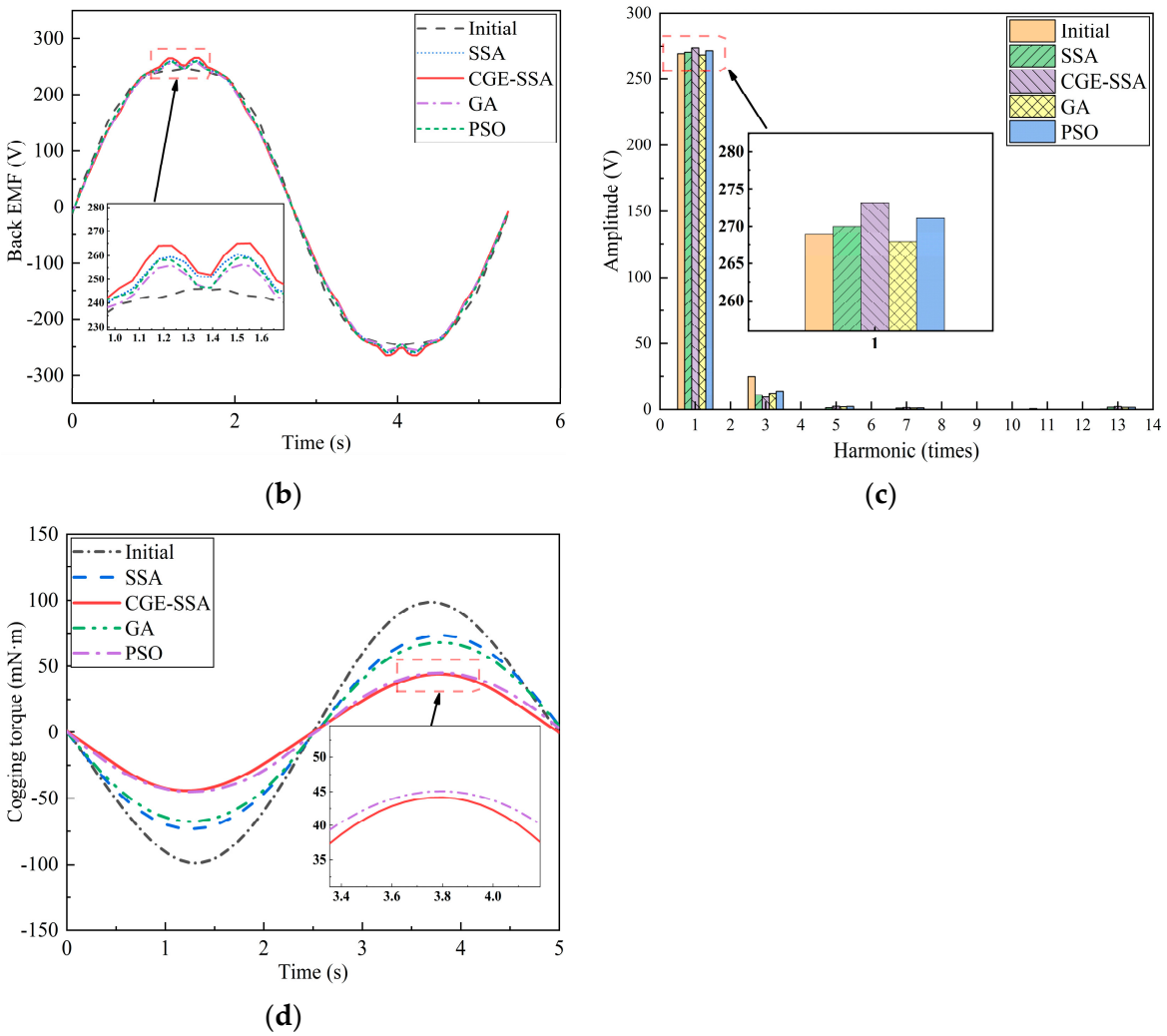


Figure 15. Comparison of optimization results: (**a**) output torque comparison; (**b**) back EMF comparison; (**c**) back EMF harmonic comparison; and (**d**) cogging torque comparison.

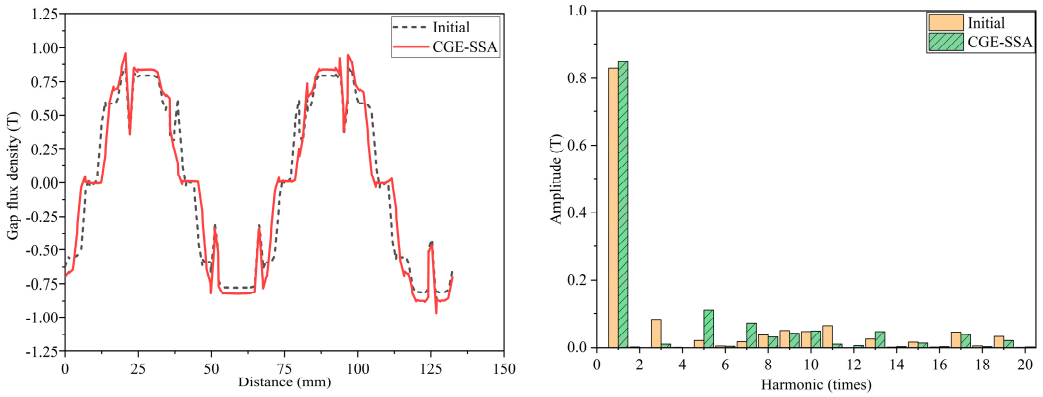
The torque pulsation was analyzed using the analytical method, and the expression for the relationship between the torque ripple and the air-gap density harmonics was obtained using Equation (11), as follows:

$$T_r = -\frac{\mu_0}{g} prL\pi \sum_{\substack{h = 10m \pm 1 \\ m = 1,2,3}}^{\infty} [hF_{sh}F_{rh}\sin((h \pm 1)\omega t \mp \gamma_d)] \quad (11)$$

where μ_0 is the air permeability; g is the air-gap length; p is the number of rotor pole pairs; r is the radius of the air gap in the middle layer; L is the axial length of the motor; F_{sh} is the coefficient of the hth stator magnetomotive force; F_{rh} is the coefficient of the hth rotor magnetomotive force; ω is the electric angular velocity; t is the time; and γ_d is the current angle of the d-axis.

In Equation (11), it can be seen that the air-gap magnetization that generates the torque ripple is mainly the 10 m ± 1th harmonic, of which the most dominant are the 9th and 11th harmonics. As can be seen from the comparison of the results before and after optimization in Figure 16, the harmonic content of the no-load air-gap magnetism is richer, and the amplitudes of the 9th harmonic and 11th harmonic after optimization decrease, from 0.048 T and 0.0625 T to 0.04 T and 0.01 T, respectively, effectively suppressing torque

pulsation. The optimized motor's air-gap magnetism is significantly improved, the air-gap magnetism amplitude increases, from 0.87 T to 0.96 T, and this increase can effectively improve the output capacity of the motor, indirectly improving its efficiency.



(**a**) (**b**)

Figure 16. Comparison before and after optimization: (**a**) air-gap magnetic density comparison and (**b**) harmonic comparison.

6. Conclusions

In this study, in order to realize the design and optimization of a permanent magnet water pump motor, we proposed a multi-objective optimization strategy based on the response-surface method and improved sparrow algorithm. The comparative analysis concludes that the torque pulsation was effectively reduced and the reverse electromotive force magnitude was improved to a level satisfying the output.

Compared with the traditional water pump motor design, which relies on the maximum output capacity of the pump to determine the design parameters of the motor, we tested the output capacity of the pump during actual operation to determine the design parameters of the motor, effectively reducing the size of the motor. Furthermore, in order to improve the optimization of permanent magnet synchronous motors, we improved the sparrow algorithm through the introduction of three methods: circular sinusoidal chaotic mapping, the improved sinusoidal gold strategy, and uniformly distributed adaptive weighting coefficients. Using these methods, we were able to address the disadvantages of the traditional sparrow algorithm, such as poor global optimization ability and easily falling into the local optimum. The test function optimization results demonstrate smaller standard deviation and mean values in the process of optimization for CGE-SSA compared to the SSA, GA, and PSO in terms of convergence speed, convergence progress, and optimization stability. The optimization results of the water pump motor show that the CGE-SSA-optimized motor demonstrated an improved performance with regards to torque ripple and back EMF amplitude than those optimized with SSA, GA, and PSO. The torque ripple of the motor optimized using CGE-SSA decreased, from 6.62% to 3.11%, a decrease of 53%; the back EMF amplitude increased, from 245.2 V to 265.01 V; and the aberration rate of the back EMF decreased, from 9.2% to 3.8%, effectively improving the sinusoidal degree of back EMF waveform. At the same time, the cogging torque was significantly reduced, greatly improving the vibration and noise of the motor. The optimized air-gap magnetic density amplitude increased by 0.09 T, effectively improving the overall output capability of the motor. While using other algorithms for optimization, the torque pulsation was as low as 3.92%, the counter electromotive force amplitude as high as 260.6 V, and the distortion rate as low as 4.2%; therefore, it is obvious that CGE-SSA optimization is more effective.

A comparison of the results before and after optimization proves that CGE-SSA demonstrates a better optimization effect than traditional SSA, GA, and PSO, and the motor performance is greatly improved, which verifies the feasibility and effectiveness of the opti-

mization method proposed in this paper. Although the performance was greatly improved, the improved sparrow algorithm still has shortcomings in terms of execution complexity; therefore, this paper will be followed by a further simplification of the program's implementation, in order to improve the speed of computation.

Author Contributions: Conceptualization, W.P. and P.X.; methodology, W.P.; software, W.P.; validation, W.P., Z.L. and A.L.; formal analysis, W.P.; investigation, Z.L.; resources, J.P.; data curation, W.P.; writing—original draft preparation, W.P.; writing—review and editing, P.X.; visualization, W.P.; supervision, W.P.; project administration, P.X.; funding acquisition, J.P. All authors have read and agreed to the published version of the manuscript.

Funding: This research was supported by the Key Research and Development Projects in Anhui Province (2022a05020007), and the National Natural Science Foundation of China (52375227).

Institutional Review Board Statement: Not applicable.

Informed Consent Statement: Not applicable.

Data Availability Statement: All data are contained within the article.

Conflicts of Interest: The authors declare no conflicts of interest.

References

1. Zhang, Y.M.; Li, J.X.; Feng, Z.Y.; Peng, S.J.; Zhao, S.D. Research on multi-objective optimization of automotive electronic water pump motor considering the factor of gap viscous loss. *Struct. Multidiscip. Optim.* **2022**, *65*, 243. [CrossRef]
2. Lu, R.; Yuan, J.P.; Wang, L.Y.; Fu, Y.X.; Hong, F.; Wang, W.J. Effect of volute tongue angle on the performance and flow unsteadiness of an automotive electronic cooling pump. *Proc. Inst. Mech. Eng. Part A J. Power Energy* **2021**, *235*, 227–241. [CrossRef]
3. Choi, K.W.; Kim, K.B.; Lee, K.H. Investigation of emission characteristics affected by new cooling system in a diesel engine. *J. Mech. Sci. Technol.* **2009**, *23*, 1866–1870. [CrossRef]
4. Shin, Y.H.; Kim, S.C.; Kim, M.S. Use of electromagnetic clutch water pumps in vehicle engine cooling systems to reduce fuel consumption. *Energy* **2013**, *57*, 624–631. [CrossRef]
5. Jeon, H.; Hyun, D.; Lee, H.; Son, S.; Han, J. Optimization of Blades and Impellers for Electric Vehicle Centrifugal Pumps via Numerical Analysis. *Energies* **2024**, *17*, 853. [CrossRef]
6. Lim, D.H.; Kim, S.C.; Kim, M.S. Thermal anaysis of an electric water pump for internal combustion engine vehicles. *Int. J. Automot. Technol.* **2013**, *14*, 579–585. [CrossRef]
7. Xu, W.; Xu, J.; Zhang, W.H.; Wang, J.Y. A combined-pole permanent magnet synchronous motor incorporating nanocomposite magnets. *J. Magn. Magn. Mater.* **2023**, *577*, 170807. [CrossRef]
8. Song, T.F.; Liu, H.J.; Zhang, Q.; Zhang, Z.Y. Multi-physics and multi-objective optimisation design of interior permanent magnet synchronous motor for electric vehicles. *IET Electr. Power Appl.* **2020**, *14*, 2243–2254. [CrossRef]
9. Mutluer, M.; Bilgin, O. An intelligent design optimization of a permanent magnet synchronous motor by artificial bee colony algorithm. *Turk. J. Electr. Eng. Comput. Sci.* **2016**, *24*, 1826–1837. [CrossRef]
10. Ergene, L.T.; Polat, A.; Bakhtiarzadeh, H. Design of a permanent magnet synchronous motor used in elevators. *J. Fac. Eng. Archit. Gazi Univ.* **2018**, *33*, 725–737.
11. Ghoroghchian, F.; Aliabad, A.D.; Amiri, E. Design and analysis of consequent-pole line start permanent magnet synchronous motor. *IET Electr. Power Appl.* **2020**, *14*, 678–684. [CrossRef]
12. Wang, Y.H. Design Study of Electronic Water Pump Motor for New Energy Vehicles. Master's Thesis, Liaoning University of Technology, Liaoning, China, June 2020.
13. Xu, X.H. Structural Design and Optimization of Electronic Water Pump for Automotive Cooling. Master's Thesis, Chongqing University of Technology, Chongqing, China, March 2021.
14. Monjezi, S.R.; Kiyoumarsi, A.; Mirzaeian Dehkordi, B.; Sabahi, M.F.; Vafaie, M.H. Shape Design Optimization of Interior Permanent-Magnet Synchronous Motor with Machaon Flux Barriers for Reduction of Torque Pulsation. *Electr. Power Compon. Syst.* **2016**, *44*, 2212–2223. [CrossRef]
15. Kim, K.H.; Park, H.I.; Jang, S.M.; Choi, J.Y. Comparison of Characteristics of Double-Sided Permanent-Magnet Synchronous Motor/Generator According to Magnetization Patterns for Flywheel Energy Storage System Using an Analytical Method. *IEEE Trans. Magn.* **2015**, *51*, 4.
16. Liu, G.H.; Zeng, Y.; Zhao, W.X.; Ji, J.H. Permanent Magnet Shape Using Analytical Feedback Function for Torque Improvement. *IEEE Trans. Ind. Electron.* **2018**, *65*, 4619–4630. [CrossRef]
17. Ilka, R.; Alinejad-Beromi, Y.; Yaghobi, H. Cogging torque reduction of permanent magnet synchronous motor using multi-objective optimization. *Math. Comput. Simul.* **2018**, *153*, 83–95. [CrossRef]

18. Hao, Z.Y.; Zhou, W.S.; Ji, T.P.; Huang, X.Z.; Zhang, C.M. Multi-Objective Optimization of Double Primary Tubular Permanent Magnet Synchronous Linear Motor in Wide Temperature Range Environment Based on Pareto Front Method. *IEEE Access* **2020**, *8*, 207193–207203. [CrossRef]
19. Lim, D.K.; Yi, K.P.; Jung, S.Y.; Jung, H.K.; Ro, J.S. Optimal Design of an Interior Permanent Magnet Synchronous Motor by Using a New Surrogate-Assisted Multi-Objective Optimization. *IEEE Trans. Magn.* **2015**, *51*, 1–4.
20. Chen, Q.P.; Min, S.L.; Xu, Z.H.; Zheng, Z.Y.; Zhong, C.P.; You, D.L.; Jiang, Z.Q. Multi-objective optimization design of electric vehicle in-wheel motor based on Taguchi method. *Proc. Inst. Mech. Eng. Part D J. Automob. Eng.* **2024**, *233*, 09544070241229775. [CrossRef]
21. Song, T.F.; Zhang, Z.Y.; Liu, H.J.; Hu, W.L. Multi-objective optimisation design and performance comparison of permanent magnet synchronous motor for EVs based on FEA. *IET Electr. Power Appl.* **2019**, *13*, 1157–1166. [CrossRef]
22. Yuan, B.; Chen, P.; Wang, E.R.; Yu, J.R.; Wang, J. A Systematic Optimization Method for Permanent Magnet Synchronous Motors Based on SMS-EMOA. *Sensors* **2024**, *24*, 2956. [CrossRef]
23. Hua, Y.Z.; Zhu, H.Q.; Xu, Y. Multi-Objective Optimization Design of Bearingless Permanent Magnet Synchronous Generator. *IEEE Trans. Appl. Supercond.* **2020**, *30*, 1–5. [CrossRef]
24. Chi, S.; Yan, J.H.; Guo, J.; Zhang, J.J.; Zhang, Y.X. Multi-objective optimization design of permanent magnet linear synchronous machine based on stratified strategy. *Int. J. Appl. Electromagn. Mech.* **2023**, *71*, 237–259. [CrossRef]
25. Abroshan, A.; Hasanzadeh, S.; Fard, J.R. Multi-objective optimization of a V-type line-start PM motor based on parameter stratification and RSM. *Electr. Eng.* **2022**, *106*, 1683–1692. [CrossRef]
26. Park, J.W.; Koo, M.M.; Seo, H.U.; Lim, D.K. Optimizing the Design of an Interior Permanent Magnet Synchronous Motor for Electric Vehicles with a Hybrid ABC-SVM Algorithm. *Energies* **2023**, *16*, 5087. [CrossRef]
27. Zhang, W.Y.; Li, K.K.; Yang, X. Multi-objective optimization of flywheel motors based on parameter prioritization (in China). *J. Southwest Jiaotong Univ.* **2023**, *58*, 922–932.
28. Li, G.S.; Sun, H.Q.; Hu, W.G.; Li, Y.; Bai, Y.Q.; Guo, Y.J. Multi-Objective Optimization Design of the External Rotor Permanent Magnet-Assisted Synchronous Reluctance Motor Based on the Composite Algorithm. *Electronics* **2023**, *12*, 4004. [CrossRef]
29. Du, G.H.; Hu, C.S.; Zhou, Q.X.; Gao, W.T.; Zhang, Q.Z. Multi-Objective Optimization for Outer Rotor Low-Speed Permanent Magnet Motor. *Appl. Sci.* **2022**, *12*, 8113. [CrossRef]
30. Liu, X.; Zheng, X.L.; Wang, X.Y. Analysis of End-Effect Torque and Multi-Objective Optimization for Multi-Port Spatial Permanent Magnet Synchronous Motor. *IEEE Trans. Magn.* **2022**, *58*, 1–11. [CrossRef]
31. Xue, J.; Shen, B. A novel swarm intelligence optimization approach: Sparrow search algorithm. *Syst. Sci. Control Eng.* **2020**, *8*, 22–34. [CrossRef]
32. Ma, J.; Yu, S.; Cheng, W. Composite Fault Diagnosis of Rolling Bearing Based on Chaotic Honey Badger Algorithm Optimizing VMD and ELM. *Machines* **2022**, *10*, 469. [CrossRef]
33. Li, M.Y.; Liu, Z.L.; Song, H.X. An improved algorithm optimization algorithm based on RungeKutta and golden sine strategy. *Expert Syst. Appl.* **2024**, *247*, 123262. [CrossRef]
34. Khan, M.K.; Zafar, M.H.; Rashid, S.; Mansoor, M.; Moosavi, S.K.R.; Sanfilippo, F. Improved Reptile Search Optimization Algorithm: Application on Regression and Classification Problems. *Appl. Sci.* **2023**, *13*, 945. [CrossRef]
35. Taherkhani, M.; Safabakhsh, R. A novel stability-based adaptive inertia weight for particle swarm optimization. *Appl. Soft Comput.* **2016**, *38*, 281–295. [CrossRef]

Disclaimer/Publisher's Note: The statements, opinions and data contained in all publications are solely those of the individual author(s) and contributor(s) and not of MDPI and/or the editor(s). MDPI and/or the editor(s) disclaim responsibility for any injury to people or property resulting from any ideas, methods, instructions or products referred to in the content.